Non-Boussinesq simulations of Rayleigh–Bénard convection in a perfect gas

Frank Robinson[a)]
Astronomy Department, Yale University, Box 208101, New Haven, Connecticut 06520-8101

Kwing Chan
Department of Mathematics, The Hong Kong University of Science and Technology, Clear Water Bay, Kowloon, Hong Kong

(Received 27 August 2003; accepted 2 February 2004; published online 2 April 2004)

We present direct numerical simulations of Boussinesq and non-Boussinesq Rayleigh–Bénard convection in a rigid box containing a perfect gas. For small stratifications, which includes Boussinesq fluids, the first instability after steady rolls was an oscillatory instability (a Hopf bifurcation). The resulting convection was characterized by two hot and two cold blobs circulating each convective roll. The same sign thermal perturbations (blobs) are at diametrically opposite points on the circular rolls, i.e., they are symmetric about the roll center. The time for a hot (or cold) blob to circulate a roll was between two and three roll turnover times. When the stratification was of sufficient strength, there was a dramatic change in the nature of the bifurcation. The sign of the thermal perturbations became antisymmetric with respect to the roll center, i.e., a hot blob was diametrically opposite a cold blob. In this case, a hot or cold blob circulated around each roll in about one turnover time. In a stratified layer, the Rayleigh number varies with height. We found that at the Hopf bifurcation, the Rayleigh number at the base was closest to the Boussinesq value. The change in instability appeared to be related to an increase in the speed (or Mach number) of the circulating rolls. It did not seem to be affected by the transport property variation with temperature. If the along roll aspect ratio was less than 2 or the walls perpendicular to the roll axis periodic, then only the symmetric instability could be found. We describe how our results might be reproduced in a laboratory experiment of convection in cryogenic helium gas. [DOI: 10.1063/1.1689350]

I. INTRODUCTION

Due to the very low temperatures (≈5 K) involved in cryogenic helium convection experiments,[1,2] it is now possible to get much closer to a specific type of stratified convection, in which the vertical temperature difference ΔT is a significant fraction of the mean gas temperature T. This is one example of non-Boussinesq convection, other examples are deep mantle convection[3] or convection in the presence of strong viscocity variations.[4] At the low pressures and densities involved, the experiments can operate in the perfect gas limit.[2,5,6] This means that convection in a perfect gas, with say $\Delta T/T \approx 0.5$, can be modeled experimentally. This paper describes numerical simulations of this type of non-Boussinesq convection. To properly account for such non-Boussinesq effects, we solved the fully compressible Navier–Stokes equations in a perfect gas. To simulate laboratory conditions, the gas was enclosed in a three-dimensional box with rigid walls.

Most convection experiments work with Boussinesq fluids in which the material properties are constant and thermally induced density fluctuations provide buoyancy.[7] Early laboratory experiments typically used air or water as the working fluid,[8–10] while more recent experiments have used compressible gases, with much smaller diffusion times, and therefore a much greater range of Prandtl numbers (ratio of thermal to viscous time scale).[11] In convection experiments in water, one typically has $\Delta T/T \approx 0.01$. Such a value is within the Boussinesq regime. Past laboratory experiments have provided good benchmarks for Boussinesq studies of convection, but there are few laboratory experiments of non-Boussinesq convection.[1,4,12,13] In fact, experimentalists generally try to minimize non-Boussinesq effects in order to simplify their analysis.[14,15]

Incompressible fluids are commonly modeled using a set of partial differential equations known as the Oberbeck–Boussinesq equations.[16] The two most often used approaches to model the equations are the Galerkin method and finite difference methods.[17] Early analytical/numerical studies concentrate on the transition from the static conductive state to small amplitude convective rolls. This first bifurcation is brought about by increasing a control parameter called the Rayleigh number Ra, above a critical value Ra_c. For incompressible convection, the bifurcation to steady motion is a stationary instability. However, in the fully compressible case, the onset can be in the form of gravity waves or as an acoustic mode.[18] In the region of the critical point, as the velocity is small, linear analysis and weakly nonlinear analysis are possible.[19] Analytical studies of finite amplitude compressible convection have been done in the case of fixed heat

[a)]Electronic mail: marjf@astro.yale.edu

flux at the base of the convection layer,[20] but not in the case of fixed temperatures on the horizontal boundaries.

Highly nonlinear convection ($\mathrm{Ra} > 10\mathrm{Ra}_c$) is generally studied numerically, typically in boxes with periodic side boundaries.[21] As the characteristic time scale in liquid convection is the thermal diffusion time, while in gases it is the much shorter sound travel time, it has, until recently, been numerically prohibitive to solve the full Navier–Stokes equations near the transition from incompressible to compressible convection. Direct numerical simulations can generally be split into two groups, those of Boussinesq fluids[22] and those of fully compressible fluids.[23] In the simulations of fully compressible convection,[23,24] as periodic sides and stress free upper and lower walls were used, Rayleigh numbers of a few hundred times critical were possible. While being highly nonlinear, the convection was still laminar. There have been some numerical studies of departures from the Boussinesq approximation in the two-dimensional periodic Rayleigh–Beńard problem,[25,26] but there are few studies of the transition region between incompressible and compressible convection in real convection experiments. The numerical experiments in this paper are in boxes with rigid walls and cover the full range of stratifications of the transition region, for example, $0.02 \leqslant \Delta T/T \leqslant 0.8$.

The outline of the paper is as follows. In the first section, we describe the mathematical model and the numerical scheme. Then, we describe how well convection characteristics measured from laboratory experiments (Nusselt numbers, transition Rayleigh numbers, and oscillation periods) are reproduced by the numerical simulations. In later sections, we describe how and why stratified convection is affected by changes in the stratification or the aspect ratio, and how the results might be reproduced in cryogenic helium experiments. The final section is a conclusion.

II. NUMERICAL METHODS

A. Mathematical model

The numerical fluid is contained in a closed rectangular box. In the absence of motion, and assuming a constant thermal conductivity, the equations of compressible convection in conservation form,[27] reduce to the equations for hydrostatic and thermal equilibrium, a solution of which is

$$T/T_t = 1 + Z(1 - z/d), \tag{1}$$

$$\rho/\rho_t = (T/T_t)^m, \tag{2}$$

$$p/p_t = (T/T_t)^{m+1}, \tag{3}$$

where $Z = (T_b - T_t)/T_t$ is the external temperature contrast, z is the vertical distance from the base, d is the depth of the box, m is the polytropic index, p is the pressure, and ρ is the density. The subscripts "t" and "b" denote the top and bottom of the box. This is the *initial state* of the gas. Equations (1)–(3) describe a polytrope. The ratio of the specific heats $\gamma = c_p/c_v$, where c_p and c_v are the specific heats at constant pressure and volume, respectively. γ and m determine the convective stability of the layer. For an inviscid fluid, the layer is convectively unstable if

$$\frac{d(\ln T)}{d(\ln p)} - \frac{d(\ln T)}{d(\ln p)_{\mathrm{ad}}} > 0. \tag{4}$$

Using Eq. (3) and the equation for an adiabatic process,

$$p \propto T^{\gamma/\gamma - 1}, \tag{5}$$

for the first and second parts of Eq. (4), the instability criterion reduces to

$$m < 1/(\gamma - 1). \tag{6}$$

Equations (1)–(3) provide a reference atmosphere from which convenient dimensionless units can be formed. Length is scaled by d, and time by $d/\sqrt{(p_t/\rho_t)}$. p_t and ρ_t are the pressure and density at the top of the box. In such units, velocity v is scaled by the isothermal sound speed, $c_t = \sqrt{p_t/\rho_t}$ and the acceleration due to gravity g is scaled by c_t^2/d. In the rest of the paper, unless otherwise specified, all quantities are nondimensional.

Using the nondimensional forms of Eqs. (1) and (3) that describe the initial polytrope, gives

$$\frac{dp}{dz} = \frac{dp}{dT} \cdot \frac{dT}{dz} = -(m+1)T^m \cdot Z. \tag{7}$$

As the initial layer is in hydrostatic equilibrium

$$\frac{dp}{dz} = -\rho g. \tag{8}$$

Combining Eqs. (7) and (8) gives

$$g = (m+1)\frac{pZ}{\rho T}, \tag{9}$$

which for the nondimensional perfect gas equation, $p = \rho T$, becomes

$$g = (m+1)Z. \tag{10}$$

As g depends on m and Z, it is not an independent parameter. The horizontal sides of the box are scaled by the dimensional depth d, so that $L_x = \Gamma_x d$ and $L_y = \Gamma_y d$. Here Γ_x and Γ_y are known as the aspect ratios, and L_x and L_y are the geometric lengths perpendicular parallel to the roll axis.

With the above scalings, the governing equations become

$$\partial\rho/\partial t = -\nabla \cdot \rho\mathbf{v}, \tag{11}$$

$$\partial\rho\mathbf{v}/\partial t = -\nabla \cdot \rho\mathbf{v}\mathbf{v} - \nabla p + C_\mu[\nabla^2\mathbf{v} + \tfrac{1}{3}\nabla(\nabla \cdot \mathbf{v})] - \rho(m+1)Z\mathbf{e_k}, \tag{12}$$

$$\frac{\partial E}{\partial t} = -\nabla \cdot [(\rho T/(\gamma - 1) + p + \rho v^2/2)\mathbf{v} - \mathbf{v} \cdot \boldsymbol{\Sigma}] + \nabla \cdot \left[\frac{C_\mu \gamma}{(\gamma - 1)\mathrm{Pr}}\nabla T\right] - \rho\mathbf{v} \cdot (m+1)Z\mathbf{e_k}, \tag{13}$$

$$p = \rho T, \tag{14}$$

where $\mathbf{e_k}$ is a unit vector directed vertically upwards.

The viscous stress tensor $\Sigma_{ij} = C_\mu(\partial v_i/\partial x_j + \partial v_j/\partial x_i) - (2C_\mu/3)(\nabla \cdot \mathbf{v})\delta_{ij}$.[28] Additional terms in the equations are the nondimensional dynamic viscosity C_μ and the Prandtl

number Pr. As $C_\mu=\mu/(c_t d\rho_t)$ (where μ is the dimensional dynamic viscosity), it is equal to the ratio of the sound crossing time, $d/\sqrt{p_t/\rho_t}$, to the viscous diffusion time, $d^2\rho_t/\mu$.

The total energy per unit volume E in a fluid parcel, equals the internal energy per unit volume $\rho T/(\gamma-1)$, plus the kinetic energy per unit volume of the fluid parcel $\rho v^2/2$. Equation (13) describes the time rate of change of E. The right-hand side consists mainly of fluxes of energy in or out of the control volume by different physical processes. Considering the terms operated on by $\nabla\cdot$ operator consecutively, the first two terms added together represent the enthalpy flux (sometimes called the convective flux), the third term is the kinetic energy flux, the fourth is the viscous flux, and the fifth is the conductive heat flux. The last term in the energy equation is the work done by gravity. Equations (11)–(14) are the coded equations. A particular compressible convection experiment can be defined by specifying seven nondimensional parameters, C_μ, Pr, Z, m, γ, Γ_x, and Γ_y.

The compressible Rayleigh number Ra must take into account both the stability criterion Eq. (6), and the variation of fluid properties with depth. For the initial polytrope, $\alpha=1/T$, $\nu=C_\mu/T^m$, and $\kappa=\nu/\mathrm{Pr}$. This means the compressible Rayleigh number is

$$\mathrm{Ra}=\frac{gZ\mathrm{Pr}}{C_\mu^2}T^{2m-1}(1-(\gamma-1)m)/\gamma. \tag{15}$$

T^{2m-1} and $(1-(\gamma-1)m)/\gamma$ account for the fluid property variation with depth, and the static stability criteria, respectively.

To define a particular convection experiment, we must specify Ra at some point in the box. Using Eq. (10) and the fact that $T=1$ at the top, we define Ra at the top of the box as

$$\mathrm{Ra}_t=\frac{(m+1)Z^2\mathrm{Pr}}{C_\mu^2}(1-(\gamma-1)m)/\gamma, \tag{16}$$

where the subscript t denotes top.

We can now define a particular compressible convection experiment by specifying Ra_t, Pr, Z, m, γ, Γ_x, and Γ_y. Rearranging Eq. (16) gives

$$C_\mu=\sqrt{\mathrm{Pr}(m+1)Z^2(1-(\gamma-1)m)/\gamma\mathrm{Ra}_t}. \tag{17}$$

This suggests that characteristic time scales such as the thermal relaxation time, or the oscillation time period, will lengthen as the stratification (i.e., Z) is reduced. Solving the fully compressible equations can be very time consuming for small stratifications.

Unless otherwise stated, all surfaces are rigid ($\mathbf{v}=\mathbf{0}$), the sides are insulating ($\partial T/\partial n_j=0$, where n_j is the normal direction to the side wall), and the top and bottom surfaces are perfect conductors.

B. Numerical schemes

The coded equations were solved in three dimensions using finite differences. The numerical scheme we used was the alternating direction implicit method on a staggered mesh.[27] This method was applied to the direct numerical simulation of both steady and time-dependent flows in a perfect gas. The method has also been applied to nonideal gases, for example, to model granulation in the Sun.[29] For computation of steady flows, time accuracy is unimportant and the implicit time-stepping method can be employed. Using an implicit method, the restriction on the time step (for accuracy) comes from the flow speed (which is small for subcritical flows), rather than the sound speed. This allowed a Courant–Friedrichs–Lewy number of about 5.

In time-dependent calculations, the implicit scheme was used to relax the convection layer. Relaxation was indicated by regular periodic oscillations of the ratio of the vertical heat flux at the top, to that at the base. Once the layer was relaxed, a more accurate explicit code took over, incorporating second-order predictor–corrector (Adams–Bashforth) time integration. For computations on a $140\times60\times60$ ($x\times y\times z$) grid on the ORIGIN2000, the explicit scheme required 8 s of central processing unit (CPU) time per time step. The implicit code needed about 24 s per integration step, but it can use a 25 times larger time step. Though the implicit scheme has the advantage of allowing a large time step, there is also heavy numerical damping of the signal. To ensure that the numerical damping did not alter the final equilibrium, the two highest Rayleigh number flows were also run from start to finish using only the explicit code. We found little difference between a combined implicit–explicit computation and a purely explicit computation. The computed bifurcation points and frequencies were the same to at least two significant figures.

III. RESULTS

A. Boussinesq convection

1. Steady rolls

The first Boussinesq simulation was of the interferometric experiment by Farhadieh and Tankin.[9] In their experiment, Pr, Γ_x, and Γ_y, were 6.8, 32, and 12, respectively. As the experiment used an incompressible liquid (water), we set Z equal to 0.02 (small temperature contrast), m equal to 0 (constant density in the initial state), and γ equal to 1.1. The choice of m equal to 0 is the most appropriate for an incompressible fluid, as in the initial polytrope, $\rho\propto T^m$. Note, as $p=(\gamma-1)e$ (where e is the specific internal energy), if γ equals 1 the pressure is zero. The choice of 1.1 is close to the value of γ for water at normal temperatures.[28] This choice of parameters ensures the transport properties are nearly constant throughout the gas. Provided the stratification is small, this is true for both the initial state, and the relaxed state of the fluid. For larger stratifications, it may only be true for the initial layer.

The number of grid points across sides of lengths 32, 12, and 1, respectively, and the corresponding Nusselt number (Nu), are given in Table I. The steady state was reached, once the average Nusselt number at the cold and hot wall were within six significant figures of each other. As the experimental value of Nu was 1.45, the numerical convergence suggests a $160\times20\times20$ grid should be adequate at these low Rayleigh numbers. For Ra=6450, we found that Nu was

TABLE I. Grid refinement study: Nusselt number Nu dependency on mesh resolution for Ra equal to 2410. The first column is the number of grid points in the $x\times y\times z$ direction and the second is the computed Nusselt number. The experimental value was 1.45.

Grid	Nu
80×20×15	1.514
160×20×15	1.454
320×20×15	1.445
160×30×15	1.444
160×20×10	1.544
160×20×20	1.447

exactly 2.18 on a 160×20×20 grid. This is the same as the value of Nu recorded in the laboratory experiment.

In a region close to the critical point Ra_c, the Nusselt number should grow linearly with $(\mathrm{Ra}-\mathrm{Ra}_c)/\mathrm{Ra}_c$.[30] By measuring Nu for Ra just above Ra_c, and extrapolating to unit Nu, we found Ra_c to be about 1709. For an infinite layer with rigid top and bottom boundaries, $\mathrm{Ra}_c=1707.76$. The experimental value[9] was 1700 ± 20.

2. Oscillatory rolls

In one of the convection experiments by Gollub and Benson,[8] the external temperature gradient was increased until a supercritical Hopf bifurcation[31] from steady to oscillatory convection occurred. The corresponding numerical simulation was done on a 70×30×30 grid, along sides with aspect ratios, 3.5, 2.1, and 1, respectively. To ensure adequate resolution, the simulations with the highest Ra (which had the thinnest thermal boundary layers), were also computed on a 140×60×60 grid. The flow character was unchanged. The parameters Pr, Z, m, and γ, were 2.5, 0.02, 0, and 1.1, respectively.

The initial flow perturbation was a pair of two-dimensional rolls, parallel to the shorter side. When Ra was above 30 000, and the numerical fluid had relaxed, the fluid velocity varied sinusoidally with a constant amplitude and frequency. To locate the bifurcation point, the amplitude of the vertical velocity was measured for different Rayleigh numbers. Starting at 31 000, Ra was incremented in steps of 2000. In the experiments, when the temperature was increased, the fluid required several thermal diffusion times to reach a steady state.[32] Each numerical simulation took about 50 h of CPU time on the ORIGIN 2000 to reach the next equilibrium (or asymptotic state). At each stage, once the flow had relaxed, the vertical component of velocity at the center and left-hand side of the box, were measured. Results were taken only after the oscillation frequency measured at the side, matched the value at the center of the box, to two decimal places. Once the flow has relaxed, the frequency was found to be independent of position.

Close to the bifurcation point, the oscillation amplitude squared shows a linear dependence on the distance of the Rayleigh number from the Hopf bifurcation point. This functional dependence is consistent with stability theory for a horizontally infinite layer.[33] It appears that it is still valid for small aspect ratio containers. The Hopf bifurcation point can be found by extrapolating to zero amplitude. This marks the transition from steady rolls to oscillatory convection. The bifurcation point computed this way was about 29 150. In Gollub and Benson,[8] Ra was expressed in units of the critical Rayleigh number in an infinite layer, Ra_c. The relative Rayleigh number at the bifurcation point was $\mathrm{Ra}/\mathrm{Ra}_c=17\pm1$ and $\mathrm{Ra}_c=1707.76$. Thus, the experimental value was $29\,000\pm1708$, in excellent agreement with our result. For a Rayleigh number of about 35 000, Gollub and Benson recorded an oscillation frequency of about 25 (in units of inverse thermal diffusion times). We found a value of 23.8.

B. Non-Boussinesq convection

In most experiments, the Rayleigh number is increased further until the next bifurcation is found. Instead of this, we increased the initial stratification (by increasing either Z or m), used a value of Ra large enough to be in the oscillatory regime, and ran the new simulation to its asymptotic state. Once we had found steady oscillations, we estimated the bifurcation point in the same manner as in the previous section. We shall denote the walls parallel and perpendicular to the roll axis, respectively, as the side walls and the end walls. Unless otherwise stated, all simulations from now on, are done in a 3.5×2.1×1 box with rigid walls.

Convection characteristics for various stratifications in boxes with rigid walls, are given in Table II. The last row is for a resolution of 140×60×60, while the other simulations each have a resolution of 70×30×30. The superscript "h" denotes high resolution. Column 3 is the Rayleigh number evaluated at the top of the box, Ra_t. Columns 4 and 5 are the Rayleigh number at the Hopf bifurcation point Ra_h, measured at the midplane (mp), and at the bottom (bm) of the box. As the Hopf bifurcation point was only computed for simulations in which the polytropic index was zero, the other simulations have no entries in columns 4 and 5. The results in column 4 suggest that increasing the temperature contrast Z from 0.02 to 0.8 causes the Hopf bifurcation to occur at a higher Rayleigh number. However, column 5 suggests that the transition Rayleigh number at the bottom is almost *independent of the temperature stratification*. At the Hopf bifurcation, the Rayleigh number at the base, most closely resembles the Boussinesq value. (Note the Rayleigh numbers in Table II are only given to two significant figures.)

Columns 6 and 7 are concerned with the criteria for a Boussinesq fluid.[34] For a Boussinesq fluid both $\alpha\Delta T$ and d/H_p are much less than unity. The quantities α and H_p, are the volume expansion coefficient at constant pressure and the isothermal pressure scale height (in dimensional units) of the initial polytrope, respectively. For a slightly compressible perfect gas, α is close to the reciprocal of the temperature at the center of the layer. As the temperature at the midplane of the initial polytrope is $1+Z/2$,

$$\alpha\Delta T\approx Z/(1+Z/2), \tag{18}$$

while Eq. (3) implies that

$$d/H_p\approx(m+1)\ln(1+Z). \tag{19}$$

Turbulent convection experiments in liquid helium[5] found non-Boussinesq effects if $\alpha\Delta T$ was about 0.4.

TABLE II. Simulations of stratified Rayleigh–Beńard convection in a box of dimensions 3.5×2.1×1, with impenetrable nonslip side walls. Experimental values of temperature contrast Z; polytropic index m; Rayleigh number at the top Ra_t; Rayleigh number for the Hopf bifurcation evaluated at the midpoint Ra_h (mp) and at the bottom Ra_h (bm); product of volume expansion coefficient at constant pressure and temperature change over the layer $\alpha\Delta T$; ratio of box depth to pressure scale height d/H_p; oscillation time period T_{osc}; root-mean-square velocity V_{rms}; ratio of turn-over time to oscillation period $T_{\mathrm{TOT}}/T_{\mathrm{osc}}$; wavelength of the oscillations that travel along the roll axis λ_y; relative variation of kinematic viscosity with depth $\Delta\overline{\nu}/\overline{\nu}_{\mathrm{mp}}$ and relative variation of α with depth. The values of $\alpha\Delta T$ and d/H_p are for the initial stratification, while $\Delta\overline{\nu}/\overline{\nu}_{\mathrm{mp}}$ and $\Delta\overline{\alpha}/\overline{\alpha}_{\mathrm{mp}}$ are computed from the relaxed (convecting) state. The overbar denotes a horizontal and temporal average, the mp denotes evaluation at the midplane. The computation in the last row (with the superscript h) was performed on a 140×60×60 grid, while all the others were computed on 70×30×30 grids. By comparing the last row and the seventh row, we can see that the lower resolution is adequate. The results are taken after the flow has relaxed.

Z	m	Ra_t	Ra_h (mp)	Ra_h (bm)	$\alpha\Delta T$	d/H_p	T_{osc}	V_{rms}	$T_{\mathrm{TOT}}/T_{\mathrm{osc}}$	λ_y	$\Delta\overline{\nu}/\overline{\nu}_{\mathrm{mp}}$	$\Delta\overline{\alpha}/\overline{\alpha}_{\mathrm{mp}}$
0.02	0	35 000	29 000	29 000	0.02	0.02	656	0.0023	2.7	2.4	0.01	0.02
0.04	0	35 000	29 000	29 000	0.04	0.04	330	0.0044	2.8	2.4	0.02	0.04
0.08	0	35 000	30 000	28 000	0.1	0.1	167	0.0085	2.8	2.4	0.04	0.08
0.32	0	37 000	31 000	28 000	0.3	0.3	44	0.032	2.8	2.4	0.13	0.28
0.64	0	47 000	35 000	28 000	0.5	0.5	53	0.061	1.2	1.2	0.23	0.53
0.8	0	52 000	36 000	28 000	0.6	0.6	44	0.075	1.2	1.2	0.26	0.64
0.32	1.5	28 000	⋯	⋯	0.3	0.7	70	0.047	1.2	1.2	0.43	0.29
0.64	1.5	24 000	⋯	⋯	0.5	1.0	39	0.087	1.2	1.2	0.78	0.54
0.32^h	1.5	28 000	⋯	⋯	0.3	0.7	68	0.048	1.2	1.2	0.43	0.29

Column 8 in Table II is the oscillation period T_{osc} measured from the velocity time series at an arbitrary point in the box. Column 9 is the root-mean-square (rms) velocity V_{rms} averaged over time and volume. As the velocity has been scaled by the sound speed, V_{rms} provides an estimate of the Mach number (ratio of flow speed to sound speed). Column 10 is an estimate of the number of complete oscillations occurring in one roll circulation. The turnover time T_{TOT} was estimated as $4/V_{\mathrm{rms}}$. The validity of this estimate is shown in Sec. III B 2. Column 11 is the wavelength λ_y of the standing waves, that oscillate perpendicular to the roll axis. The measurement of the wavelength is described in Sec. III B 3.

The last two columns are the fractional variation of the kinematic viscosity and the volume expansion coefficient at constant pressure. These are all computed from the relaxed simulation. The overbar denotes a combined horizontal and temporal average, and the subscript ''mp'' signifies that the denominators were evaluated at the midplane. The variation in kinematic viscosity with depth is due to the change in density with depth. Even if the density is constant in the initial state (i.e., for the cases with $m=0$), it is not constant when the fluid is relaxed. As the Prandtl number is constant, the thermal diffusivity has exactly the same variation with depth as the molecular diffusivity.

The main inferences that can be drawn from Table II are the following:

(1) There is a significant change in the dynamical character of the flow when $d/H_p \geqslant 0.5$.
(2) The value of $T_{\mathrm{TOT}}/T_{\mathrm{osc}}$ approximately halves, when the wavelength halves.
(3) The rms velocity (or Mach number) increases with increase in stratification.
(4) The oscillation period is inversely proportional to the rms velocity.

These observations suggest that the roll circulation time and the period of the oscillations are directly related. During the time of a single roll circulation, there are between two and three full oscillations in the first four simulations, while for the remaining simulations there is only about one oscillation. The change in oscillation mode is accompanied by a halving of the wavelength of the standing waves formed parallel to the roll axis. For low stratifications, the preferred wavelength is 2.4, while for high stratifications the preferred wavelength is 1.2.

1. Boundary conditions at the side walls

If the walls perpendicular to the roll axis are rigid, then waves that travel along the rolls are reflected at the walls, and standing waves (SWs) are created. If the same walls are replaced by periodic boundaries, then either SWs or traveling waves (TWs) are allowed. The details of convection in boxes with different boundary conditions at the vertical walls, are summarized in Table III. The last two columns describe the type of wave and the wall boundary condition. The labels PP, PR, and RP denote vertical walls that are all periodic, periodic in the x-direction, and periodic in the y-direction, respectively.

The main inferences that can be drawn from the table are the following:

(1) The wavelength and the ratio $T_{\mathrm{TOT}}/T_{\mathrm{osc}}$ are close to 2 if the end walls are periodic.
(2) The change in wavelength and $T_{\mathrm{TOT}}/T_{\mathrm{osc}}$, that was found for the larger stratifications in Table II, only occurs if the walls perpendicular to the roll axis are rigid.
(3) Either SWs or TWs can occur if the walls perpendicular to the roll axis are periodic.

The wavelength of the oscillations that travel along the roll axis depend on the boundary condition at the reflecting end walls. When those walls are removed, the fluid adjusts so that a complete wavelength fills the box. As the aspect ratio is 2.1, the wavelength is very close to its maximum allowed value.

2. Estimate of turnover time

To check if $4/V_{\mathrm{rms}}$ is reasonably close to T_{TOT}, massless tracer particles were tracked over two oscillation periods,

TABLE III. Experimental values of temperature contrast Z; polytropic index m; Rayleigh number at the top Ra_t; oscillation period T_{osc}; root-mean-square velocity V_{rms}; ratio of turn-over time to oscillation period $T_{\mathrm{TOT}}/T_{\mathrm{osc}}$; wavelength of the oscillations λ_y; type of wave formed (denoted SW or TW for standing and traveling waves, respectively) and side wall boundary condition. The labels PP, PR, and RP denote vertical walls that are all periodic, periodic in the x direction, and periodic in the y direction, respectively. The results are taken after the flow has relaxed. Each box has dimensions $3.5\times2.1\times1$.

Z	m	Ra_t	T_{osc}	V_{rms}	$T_{\mathrm{TOT}}/T_{\mathrm{osc}}$	λ_y	Wave type	Boundary condition
0.08	0	35 000	173	0.01	2.3	2	SW	PP
0.32	0	37 000	45	0.038	2.3	2	TW	PP
0.64	0	47 000	25	0.071	2.3	2	TW	PP
0.32	1.5	26 000	32	0.055	2.3	2	TW	PP
0.08	0	35 000	170	0.009	2.6	1.8	SW	PR
0.64	0	47 000	49	0.067	1.2	1.6	SW	PR
0.08	0	35 000	164	0.0095	2.6	2	SW	RP
0.64	0	47 000	23.5	0.067	2.5	2	TW	RP

starting at a few random points in the box. Figure 1 shows the trajectories of three particles for the case described in the third row of Table III. The speed of the particles is proportional to the distance between the points in the figure. If the particles got too close to the viscous horizontal boundaries, then they almost came to a halt. Away from the boundaries, the particles circulated once in two oscillation periods. This agrees roughly with the value of $T_{\mathrm{TOT}}/T_{\mathrm{osc}}$ in column 7 of the third row in Table III.

3. Estimate of wavelength

To estimate the wavelength λ_y of the SWs, we computed the maximum amplitude of the vertical velocity averaged over the x direction and over time. The amplitude versus distance along the roll axis y, is plotted in Figs. 2(a)–2(d). The value of Z, m, and Ra_t for each simulation is given as a header to each plot. The variation with height h reveals that the oscillations are strongest near the midplane of the box. The wavelength is twice the distance between two minimums on either side of the central maximum. For TWs, as the whole wave passes through every point in the box, the time averaged amplitude is zero. To find the wavelength, the velocity was averaged over the x direction at one instant in time. One result is shown in Fig. 3. From the amplitude and velocity plots, it is clear that the wavelength was about 2.4 for the weak stratifications, and about 1.2 for the higher stratifications. With periodic end walls, the wave adjusted to fill the box and had a wavelength of 2, regardless of stratification.

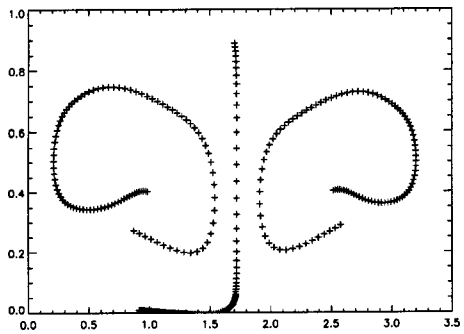

FIG. 1. Trajectories of massless tracer particles in a plane perpendicular to the roll axis that is located near the center of the box. The ordinate and abcsissa are the nondimensional vertical and horizontal sides of the box. The total time of each trajectory is two oscillation periods. The box has periodic side walls.

4. Wave number and aspect ratio dependence

The maximum growth rate for a particular oscillatory instability depends on the wave numbers parallel (α_y) and perpendicular (α_x) to the roll axis.[35] In Bolton *et al.*,[35] the value of α_y which produced the maximum growth rate was called the maximizing wave number.

If we increase the length of the box along the rolls, then the observed wavelength should gradually increase until one more half-wavelength can fit along the roll axis. Then, the corresponding wave number should jump back near the ideal value (i.e., the maximizing wave number). So for a particular simulation, while it may not be guaranteed that the wave number maximizing the growth rate will correspond to the observed wave number, because of the quantization imposed by the aspect ratio of the experiment, we could expect it to be close.

In our box of dimensions $3.5\times2.1\times1$, if the end walls were periodic, then $\lambda_y=2$. This means the wave number of the oscillations $\alpha_y=2\pi/\lambda_y$ was about 3.1. This is the same as the maximizing wave number found by Bolton *et al.* (who also employed periodic boundaries),[35] for the B02 instability with a Prandtl number of 2.5 (see Fig. 10 of Bolton *et al.*). Table IV lists experiments with different aspect ratios. By measuring V_{rms} and T_{osc}, we estimated $T_{\mathrm{TOT}}/T_{\mathrm{osc}}$. If the aspect ratio along the rolls Γ_y, was 1.5 or 1.8, then $T_{\mathrm{TOT}}/T_{\mathrm{osc}}$ was about 2.8. This was true even for higher stratifications. However, if $\Gamma_y=2.1$, 2.35, or 2.6, then the ratio $T_{\mathrm{TOT}}/T_{\mathrm{osc}}$ was about 1.2 for the highly stratified cases, while it was 2.8 for the weakly stratified cases (not shown). It seems that Γ_y needs to be bigger than 2, and the end walls rigid, for the stratification to influence the quantization of the observed wave number.

IV. ANALYSIS

For a Prandtl number of 2.5, the possible forms of oscillatory convection are cross roll, Knot, B02, BE1, Zigzag, E oscillatory, and skewed varicose.[36] Guided by the work of

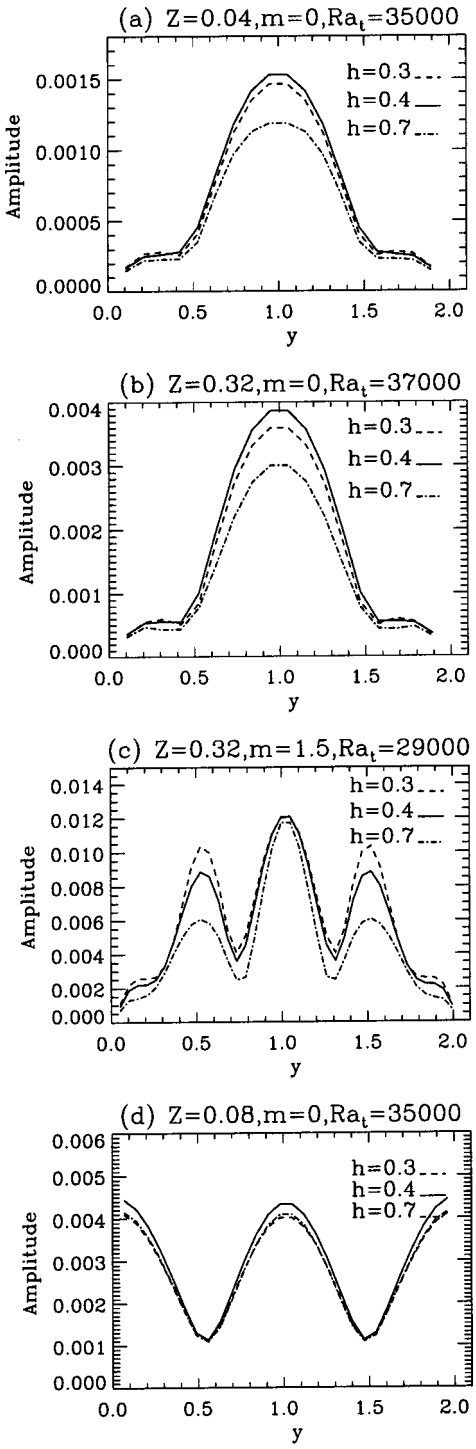

FIG. 2. Maximum nondimensional amplitude of vertical oscillations of SWs vs distance along the rolls *y*. The amplitude has been averaged over the horizontal direction perpendicular to the rolls and over time. The first three plots are for boxes with rigid boundaries, while the last is for a box with periodic boundaries. The height above the base is denoted *h*. At the top of each figure are the temperature contrast *Z*, the polytropic index *m*, and the Rayleigh number at the top, Ra_t.

Bolton *et al.*,[35] we plotted contours of the disturbance of the temperature field in the vertical plane ($y=\Gamma_y/2$) perpendicular to the roll axis. The disturbance of the temperature field is equal to the actual temperature, minus the time averaged (over one cycle) temperature.

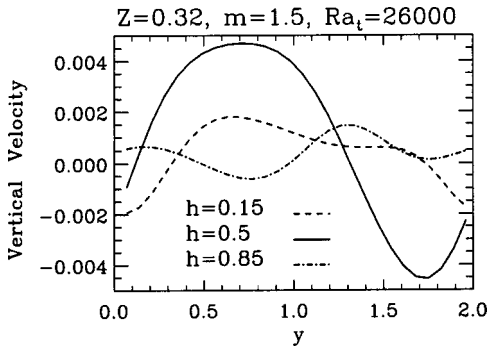

FIG. 3. Nondimensional vertical velocity averaged over the horizontal direction perpendicular to the rolls vs the distance along the rolls, *y*. The side walls are periodic. The height above the base is denoted *h*. At the top of the figure are the temperature contrast *Z*, the polytropic index *m*, and the Rayleigh number at the top, Ra_t.

For simulations in which λ_y was close to 2, the contours look like those in Figs. 4(a)–4(d). The four frames are equally spaced over one time period. As the start and end of the cycle have the same pattern, the end frame is not included. There appears to be two hot blobs (lightest regions), and two cold blobs (darkest regions), circulating around each roll. Each figure contains two adjacent rolls, the left one rotates clockwise and the right one anticlockwise. If we follow a particular blob, we can see that over the whole cycle, a blob only travels about half way round a roll, i.e., the roll turnover time is about twice the oscillation period. This type of convection looks very much like the BO2 instability.[35] Figures 5(a)–5(d) show the corresponding patterns for simulations in which λ_y was close to unity. In this case, only one hot and one cold blob circulate around each roll. A blob goes fully round a roll in one time period, i.e., the turnover time is close to the oscillation period. This type of convection looks like the BE1 instability.[35]

The main difference between the two types of instability lies in the symmetry of the temperature perturbations about the roll centers. Consider the white regions located in the bottom right and top right of Fig. 4(a). These two hot blobs are on opposite sides of the roll. This roll is spinning anticlockwise. If one considers all four frames [Figs. 5(a)–5(d)], one can see that the two hot blobs are always opposite each other. They are just like opposite spokes on a wheel. These

TABLE IV. Experimental values of temperature contrast *Z*; polytropic index *m*; along roll aspect ratio Γ_y; observed wave number along the rolls b_o; time period T_{osc}, and ratio of time period to turn-over time T_{TOT}/T_{osc}. The simulations have an aspect ratio perpendicular to the roll axis of 3.1 and rigid (no-slip) walls.

Z	m	Γ_y	b_o	T_{osc}	T_{TOT}/T_{osc}
0.08	0	1.5	4.8	174	2.8
0.08	0	2.1	2.7	167	2.8
0.08	0	2.6	2.1	163	2.8
0.32	1.5	1.8	3.1	32	2.7
0.32	1.5	2.1	5.2	70	1.2
0.32	1.5	2.35	4.7	68	1.2
0.32	1.5	2.6	4.2	66	1.3

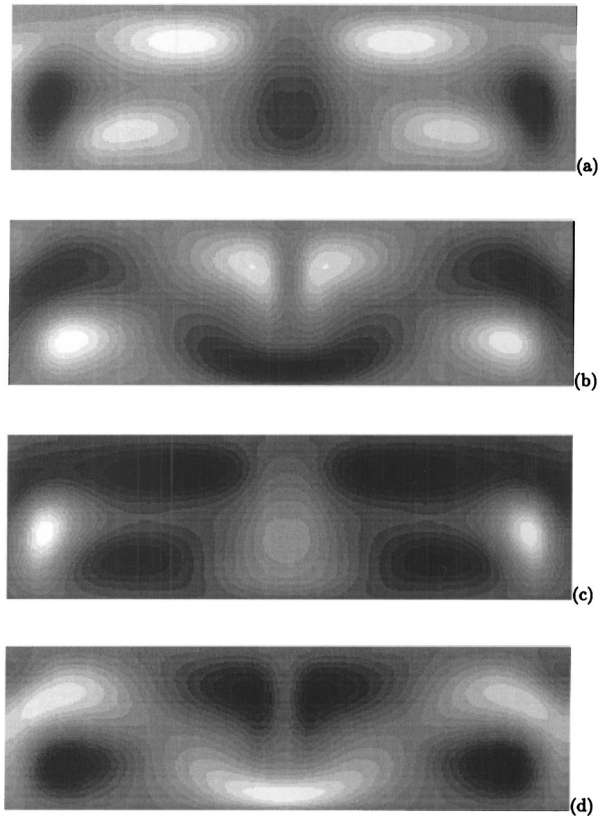

FIG. 4. Temperature disturbance in the vertical plane perpendicular to the roll axis for a typical B02 case. The frames are equally spaced over one time period. As the end of the cycle has exactly the same pattern as the first frame, it has not been included. The light and dark regions correspond to fluid that is, respectively, hotter or colder than the time averaged temperature.

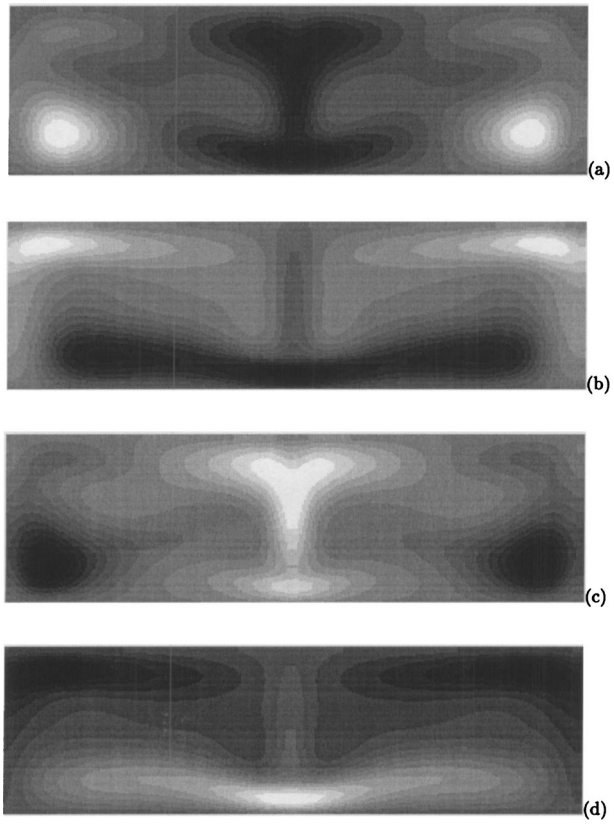

FIG. 5. Temperature disturbance in the vertical plane perpendicular to the roll axis for a typical BE1 case. The frames are equally spaced over one time period. As the end of the cycle has exactly the same pattern as the first frame, it has not been included. The light and dark regions correspond to fluid that is, respectively, hotter or colder than the time averaged temperature.

thermal perturbations are symmetric with respect to the roll center. When the stratification is increased, the symmetry is broken. In Fig. 5(a), the temperature perturbation at the bottom right-hand side (white blob) is of opposite sign to the one at the top-center (black blob). This remains true throughout the cycle. These thermal perturbations are antisymmetric with respect to the roll center.

The symmetry requirements for B02 and BE1 are described by Busse and Clever.[21] According to their criteria, the B02 mode can dominate if there is reflectional symmetry about the midplane, while the BE1 mode can prevail, if the midplane reflectional symmetry is broken.

A convection layer needs to be purely Boussinesq to have midplane reflectional symmetry. However, in a stratified fluid, there is always some asymmetry between the upflows and downflows. The amount of asymmetry depends on the amount of stratification. From Table II, it appears that the first unstable mode (after steady rolls), changed from B02 to BE1, when the physical depth of the layer was greater than about one-half an isothermal pressure scale height. While this suggests that stratification influences the instability, it does not tell us how. What we want to know is which particular property of the stratified convection, determines the dominant oscillatory instability (i.e., whether it is B02 or BE1). In the following sections, we will attempt to answer this.

A. Pressure fluctuations

For small perturbations, the equation of a perfect gas can be written as

$$\delta\rho/\rho = -\delta T/T + \delta p/p. \tag{20}$$

For a quantity q, the rms fluctuation can be computed as

$$q'' = \sqrt{\overline{q^2} - \overline{q}^2}, \tag{21}$$

where the overline denotes horizontal and temporal averaging over one oscillation period. The relative rms fluctuation $q''/\overline{q}$ is used to estimate $\delta q/q$.

Figures 6(a)–6(d), respectively, show $\rho''/\overline{\rho}$, $T''/\overline{T}$, and $p''/\overline{p}$, for four different stratifications. The values of Z, m, and Ra are given as a header to each plot. As the top and bottom surfaces were maintained at a constant temperature, the temperature fluctuations had to drop to zero there. On the other hand, pressure was free to respond to the interaction of the upflows and downflows with the horizontal surfaces. As a consequence, the pressure fluctuations were greatest near the top and bottom of the box. Near the midplane, the density and temperature fluctuations were about the same.

As the stratification was increased the pressure fluctuations, became more significant. In the last two cases, the pressure fluctuations cannot be ignored. This type of convection is non-Boussinesq. In both cases, $d/H_p \geqslant 0.5$.

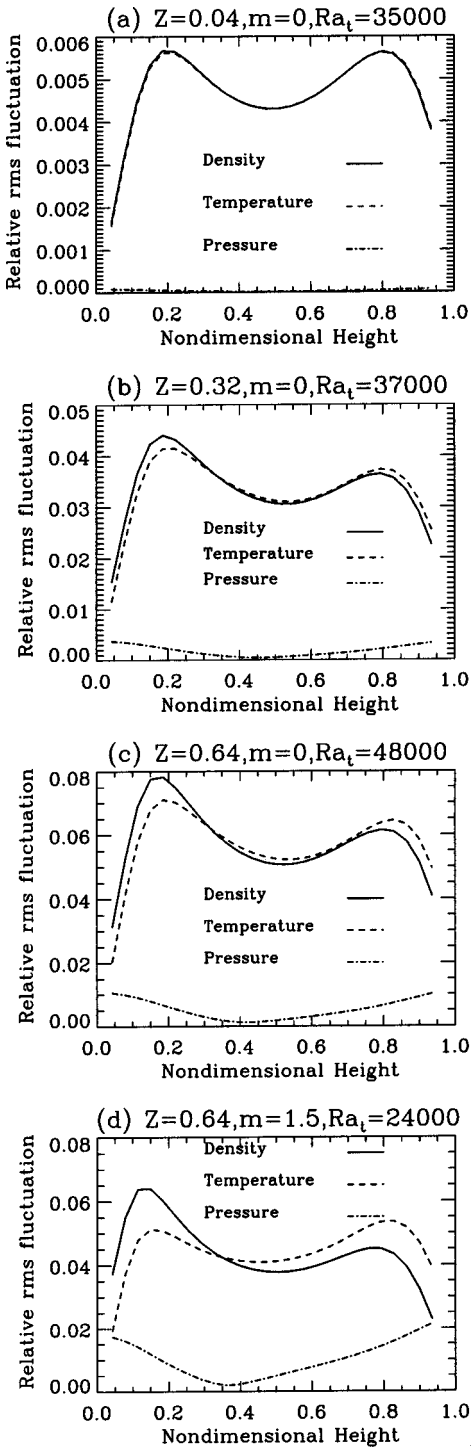

FIG. 6. Relative rms fluctuation of density, temperature, and pressure. As Z or m are increased, the contribution of pressure fluctuations to buoyancy, becomes non-negligible. At the top of each figure are the temperature contrast Z, the polytropic index m, and the Rayleigh number at the top, Ra_t.

In a box with rigid walls, the change in the nature of the convective instability from B02 to BE1 seems to be accompanied by a significant increase in the pressure fluctuations near the top and bottom of the box. This is probably because the higher stratifications have higher Mach numbers or, equivalently, faster rolls.

B. Variable thermal conductivity

To test the effect of a temperature-dependent thermal conductivity k on the BE1/B02 instabilities, we forced k in the initial layer to vary linearly with height. Keeping the parameter C_μ constant, the term in front of ∇T in Eq. (13), was multiplied by $(W+2(1-z)(1-W))$, where $W=0.9$ or 0.85 (corresponding to a 20% and 30% variation), and z is the nondimensional depth, $(0<z<1)$. We then ran some of the simulations again.

This was done for small and large stratifications. For $Z=0.04$ and $m=0$, with a 30% variation in k, the flow was almost the same, as that with no variation. As $\kappa=\kappa/\rho c_p$, this suggests the change from B02 to BE1, was probably *not* related to a change in k or κ, with depth. For $Z=0.8$, $m=0$, with a 30% variation in k, the oscillation frequency was still 44, i.e., the BE1 instability prevailed. A particular instability seemed to be stable to significant variation of k with depth.

C. Variable viscosity

Non-Boussinesq experiments of turbulent convection in glycerol, described an up–down flow asymmetry, related to the strong dependence of the viscosity on temperature.[4,12] It was shown that the velocity field adjusted, so that the stress was the same at the top and bottom boundary layers, and the temperature field adjusted, so that the top and bottom heat fluxes matched.

In our case, the kinematic viscosity ν varied with depth because of density stratification $(\nu=C_\mu/\rho)$. Could the variation of ν with depth be the reason for the change in instability? To answer this, we chose the highest stratification which exhibited the B02 instability, $(Z=0.32,\ m=0)$, and multiplied the dynamic viscosity C_μ in Eqs. (12) and (13), by $[W+2(1-z)(1-W)]$, to mimic a viscosity that increased with temperature, and by $W+2z(1-W)$ to mimic a viscosity that decreased with temperature.

The new simulations were then run to equilibrium. For $W=0.9$ and 0.85 (20% and 30% variation over the layer), with increasing or decreasing viscosity, the ratio $T_{\mathrm{osc}}/T_{\mathrm{TOT}}$ was between 2.5 and 2.8. By plotting the oscillation amplitude along the rolls (not shown), we found that these were all B02 simulations. As the flow had not changed from B02 to BE1, even when a significant viscosity variation was enforced, it does not seem that the change to BE1 is related to viscosity.

D. Flow speed

The change from B02 to BE1 seemed to be related to an increase in the speed of the flow. This produces significant pressure fluctuations. But is this the reason for the flow change? To test this hypothesis, we tried to speed up the flow without increasing the stratification. To do this, we replaced the rigid horizontal boundaries by stress free boundaries. For the stratification $Z=0.32$, $m=0$, we found that with stress free horizontal walls, the oscillation period was 65, and the turnover time was about 60. By plotting the oscillation amplitude along the roll axis (not shown), we confirmed that

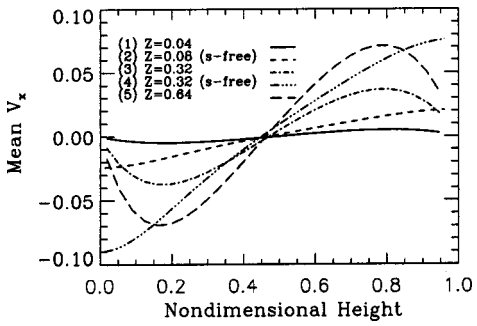

FIG. 7. Horizontal and temporal average of the horizontal velocity perpendicular to the roll axis, versus height, for five relaxed simulations. Z is the temperature contrast and each simulation has the polytropic index set to zero. The first and third simulations exhibit the B02 instability, while the rest exhibit the BE1 instability. The term *s* free denotes a simulation which has stress free horizontal boundaries.

this simulation was BE1. Additional simulations showed that, for $Z=0.16$, 0.08, 0.04 (with $m=0$), the flow was also BE1. However, if only the top was stress free, then the oscillation period was about 30 and the flow pattern was B02.

To see how the boundary condition affects the flow, the mean horizontal velocity V_x, perpendicular to the rolls, is shown in Fig. 7. The first, third, and fifth cases, all have rigid horizontal boundaries, while the second and fourth have stress free (denoted ''s-free'') boundaries. With stress free boundaries, even a small V_x is enough for BE1 to dominate. For rigid boundaries, to get BE1, the forcing or stratification, needs to be much larger. The simulation $Z=0.08$, $m=0$, with the stress free boundaries, had almost negligible pressure fluctuations. They were similar to the $Z=0.04$, $m=0$ case with rigid boundaries (see the first frame of Fig. 6). So it does not seem that pressure fluctuations caused the change from B02 to BE1. Rather, the change in instability seems to occur when the horizontal velocity close to the lower boundary exceeds a critical value.

E. Sound waves

Finally, we note that the change does not appear to be related to any acoustic phenomena. With periodic side walls, the wavelength was 2 and the highest frequency in Table III is 1/23.5. Thus,

$$\max[c_{\text{phase}}]=2/23.5\ll c_s=1. \tag{22}$$

As the phase speed c_{phase} was an order of magnitude less than the sound speed, the change from B02 to BE1 was probably not related to acoustic effects.

V. DISCUSSION: LOW-TEMPERATURE HELIUM EXPERIMENTS

One motivation of this paper was to get a benchmark for real laboratory experiments of stratified convection. Typical values of fluid properties for a cryogenic helium experiment are given in Table V.[37] The temperature at the top and bottom of the convection cell are 4 K and 6 K, respectively, and the Rayleigh number Ra is about 3×10^4.

TABLE V. Properties for a laboratory convection experiment in helium gas. Tabulated quantities are temperature T, pressure p, kinematic viscosity ν; thermal diffusivity κ; volume expansion coefficient at constant pressure α, and thermal conductivity k. The Rayleigh number Ra$\sim3\times10^4$.

T (K)	p (bar)	ν (cm^2/s)	κ (cm^2/s)	α (K^{-1})	k (W/mK)
4	1.7$E-4$	5.11	7.401	0.250	0.0077
5	2.1$E-4$	6.25	9.195	0.200	0.0096
6	2.5$E-4$	7.31	10.87	0.167	0.011

The proposed convection cell has a height of 15 cm, and the helium a mean density of 0.002 kg/m^3. At such low densities and pressures, the fluid should behave like a perfect (or ideal) gas. Using the values in Table V, we find that $\Delta p/\overline{p}$, $\Delta\nu/\overline{\nu}$, $\Delta\kappa/\overline{\kappa}$, $\Delta\alpha/\overline{\alpha}$, and $\Delta k/\overline{k}$, are 0.38, 0.35, 0.38, 0.42, and 0.34, respectively. The overbar denotes the value of a particular quantity evaluated at the mean temperature. As the variation of density with temperature, $\delta\rho/\overline{\rho}\approx\overline{\alpha}\Delta T=0.4$, the relative variation of ν and κ are probably due to the change in density with depth. This was true for the numerical simulations as well. Table I of Niemela and Sreeinivasan[6] shows that if ν is reduced by a factor of 4 then the dynamic viscosity changes by less than 1%.

In the last section, we showed that a 30% variation of k, or ν or κ, had little effect on the frequency of the oscillations. As the frequency characterizes the type of instability, we might expect the variation of k or ν in the helium experiment to have little effect on observed instability. Rather, it is the net forcing or the temperature contrast that determines the outcome. Note, in a helium experiment by Niemela *et al.*,[2] even if k was varied by 20%, the Nusselt number was hardly affected at all.

Does helium at these cryogenic temperatures behave like a perfect gas? To address this issue, the reciprocal of αT is plotted for three typical cryogenic helium experiments in Fig. 8. For a perfect (or ideal) gas, $\alpha T=1$, so that at a Rayleigh number of $\sim3\times10^4$, we should be comfortably within the perfect gas regime. It should also be possible to construct a gas tank for a polytropic gas. The dimensional acceleration

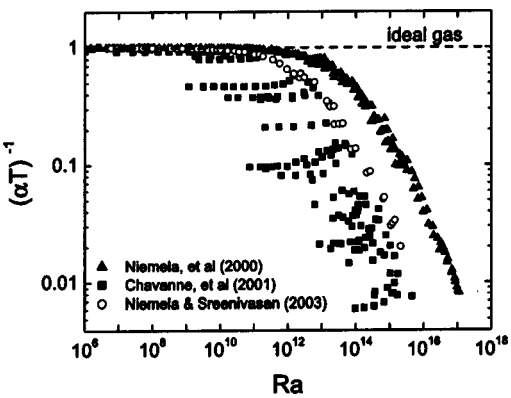

FIG. 8. The reciprocal of the product of the coefficient of volume expansion at constant pressure α and mean temperature T, as a function of Rayleigh number Ra. For a perfect (or ideal) gas $(\alpha T)^{-1}=1$. Solid squares are data of Chavanne *et al.* (Ref. 5) for a 20 cm high cell; solid circles are from Niemela and Sreenivasan (Ref. 6) for a 50 cm high cell, and open triangles are from Niemela *et al.* (Ref. 2) for a 100 cm high cell.

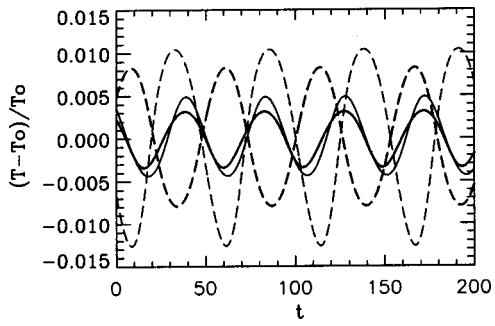

FIG. 9. Time variation of the relative temperature, $(T-T_o)/T_o$ vs time (in units of sound travel times). T is the instantaneous temperature and T_o is the time average of T. The solid and dashed lines are for a low (B02) stratification and a high (BE1) stratification, respectively. Both simulations have impenetrable no-slip walls. The thin lines denote a temperature measured at grid location (10,15,3) while the thick lines are for the temperature measured at (25,15,27). This is on a $70\times30\times30$ grid. For the low stratification, the temperature at the two points is almost in phase, while for the higher stratification the temperatures are almost completely out of phase.

due to gravity $g=(m+1)\Delta TR/d$, where R is the gas constant. In reality, g is fixed so that a polytropic distribution is nothing more than a layer with a constant temperature gradient. By adjusting the depth, total mass of gas, and temperature contrast, one should be able to generate a situation that is compatible with a certain polytropic index m. A value of m slightly greater than -1 should be accessible to experimentalists. Additional numerical simulations with $m=-0.9$ produced B02 and BE1 under conditions similar to previously documented cases. Helium gas[38] at 5.5 K and a pressure of 2.8 bar has a Prandtl number of 5. By varying the temperature or pressure, while still remaining reasonably far away from the critical point, the Prandtl number of 2.5 used in the simulations might be achievable.

How might the instabilities be observed in such experiments? Consider two points that are on diametrically opposite points of a roll at grid locations, P1=(10,15,3) and P2 =(25,15,27), on a $70\times30\times30$ grid. Figure 9 shows the relative instantaneous temperature, $(T-T_o)/T_o$ versus time (in units of sound travel times). T is the temperature at a fixed location and T_o is the time average of T. The B02 stratification ($Z=0.32$, $m=0$), has P1 and P2 denoted by thick and thin solid lines, respectively, while the BE1 stratification ($Z=0.64$, $m=0$), has P1 and P2 denoted by thick and thin dashed lines, respectively. There are three points to note from Fig. 9. First, the change in stratification from $Z=0.32$ to 0.64 does not cause much change in the time period. If both stratifications were B02, then we would expect the period to halve when Z is doubled. Second, the temperature oscillations are almost exactly in phase for the B02 case and about 180° out of phase for the BE1 case. Third, the amplitude of the oscillations is about 0.3% for the B02 case and about 1% for the BE1 case.

In the experiments, thermal probes can be placed at various locations in the cryogenic convection cell.[2] The temperature can then be accurately measured to within 1 mK. As the mean temperatures are a few K, these effects should be measurable in the actual experiments.

VI. CONCLUSION

Under laboratory conditions (i.e., in a cell with rigid walls), stratification can determine the nature of the secondary convective instability (the oscillatory instability). This is the first unstable mode after steady rolls. For small stratifications, two hot and two cold blobs circulated each convection roll. The same temperature perturbation blobs were always diametrically opposite each other on a roll. The instability produced oscillations that traveled along the roll axis. As the walls perpendicular to the roll axes were rigid, SWs were formed in the box. They had a wavelength close to the along roll length of the box. If the stratification was greater than about one-half a pressure scale height and the along-roll length greater than twice the depth, then the instability was characterized by a single hot and cold blob circulating with the convection velocity. In this case, blobs of opposite temperature perturbation were diametrically opposite, and the wavelength of the SWs was about half the along roll length of the box.

Summarizing:

(1) At the Hopf bifurcation, the Rayleigh number at the base most closely resembled the Boussinesq value of 29 000. This is in contrast to the first bifurcation (linear theory), in which the Rayleigh number at the center was closest to the Boussinesq value.
(2) The change in the nature of the secondary instability did not appear to be affected by a 30% transport property variation with temperature.
(3) While large pressure fluctuations at the base seem to accompany the change in instability, they do not appear to be the cause of the change in instability.
(4) Rather, it is the horizontal velocity near the base that seems to determines which instability prevails.
(5) Our results may be recoverable in a convection experiment in cryogenic helium.

ACKNOWLEDGMENTS

The authors wish to thank H. Ludwig, L. Li, E. W. Bolton, J. J. Niemela, H. Meyer, G. Veronis, and P. Demarque, for their contributions. One of the authors (K.C.) thanks RGC/HK for support. The authors would also like to acknowledge computer support from the Centre for High Performance Computing at Saint Mary's University in Canada. This research was supported in part by NASA Grant No. NAG5-8406 to Yale University. This work was completed at the Astronomy Unit, School of Mathematical Sciences, Queen Mary and Westfield College, London.

APPENDIX: CAN THE SAME CONVECTIVE FLOWS BE MODELED WITH THE ANELASTIC EQUATIONS?

One other commonly used set of equations sometimes used to study convection in gases are the anelastic equations.[39] The anelastic approximation assumes that the relative fluctuations in the thermodynamic variables are small and that the thermodynamic variables fluctuate over time periods of the order of the roll (eddy) turn-over time,

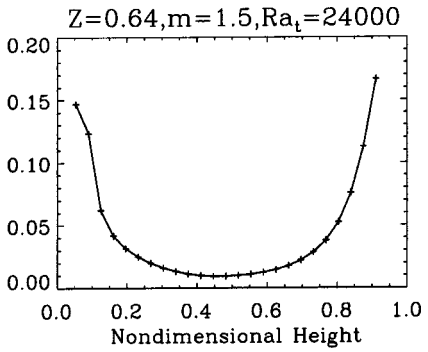

FIG. 10. Distribution of $(\partial\rho/\partial t)_{\rm rms}/(\rho\nabla\cdot\mathbf{v})_{\rm rms}$ vs height for a typical BE1 case. Individual grid points are marked by crosses. Clearly, $\partial\rho/\partial t$ is non-negligible near the top and bottom. As the anelastic approximation excludes $\partial\rho/\partial t$, it may not be able to correctly model the physics of the thermal boundary layer. At the top of the figure are the temperature contrast *Z*, the polytropic index *m*, and the Rayleigh number at the top, Ra_t.

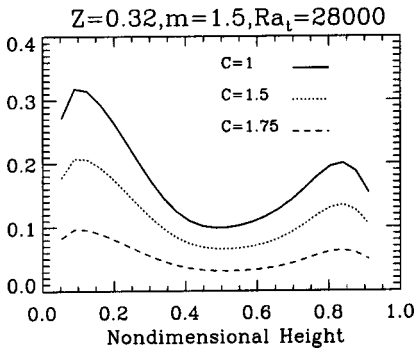

FIG. 11. $(\partial\rho/\partial t)_{\rm rms}$ divided by the depth average of density multiplied by velocity divergence $(\rho\nabla\cdot\mathbf{v})_{\rm rms}$ for three values of *C*. The parameter *C* is a factor involved in the numerical integration. The density ρ at the $(n+1)$th time step equals ρ at the *n*th time step plus $C\times\Delta t\times\partial\rho/\partial t$, where Δt is the size of the time step. At the top of the figure are the temperature contrast *Z*, the polytropic index *m*, and the Rayleigh number at the top, Ra_t.

i.e., a convective time scale. Provided the Mach number is small, the turn-over time will be much longer than the acoustic time, and it would appear that sound waves would play a minor role. One consequence of this is that the partial time derivative of density can be excluded. This allows a much larger time step to be used in numerical simulations, compared to a time step limited by acoustic motions.

In the present study, the fully compressible equations predict two types of instability, namely the two blob (BE1) and four blob (BO2) convective instabilities. To see how the anelastic equations might do in computing BE1 stratified convection, the partial time derivative of density divided by the velocity divergence multiplied by density, $(\partial\rho/\partial t)_{\rm rms}/(\rho\nabla\cdot\mathbf{v})_{\rm rms}$, is plotted for a typical highly stratified case in Fig. 10. The time derivative $(\partial\rho/\partial t)_{\rm rms}$ was computed as $-(\nabla\cdot\rho\mathbf{v})_{\rm rms}$. The plot suggests that $\partial\rho/\partial t$ is non-negligible near the top and bottom. The analysis in Sec. IV suggests that the blob instabilities are created in the horizontal thermal boundary layers. Replacing the full mass conservation law by $\nabla\cdot(\rho\mathbf{v})=0$ (as in the anelastic approximation), may mean that diverging flows at the horizontal surfaces, which seem to determine the type of instability, are incorrectly modeled. Under such conditions, the anelastic equations might not predict the same oscillatory flow as the fully compressible equations. For this reason, the anelastic approximation may have difficulty in resolving the instabilities documented in this paper. A comparison of the anelasic and compressible equations was done by Van der Borght and Fox.[40] They found marked differences between the results obtained from numerical integration of the full nonlinear compressible equations and the anelastic equations.

To investigate this topic further, we will try to mimic the anelastic equations by incrementally reducing the size of $\partial\rho/\partial t$, compared to other time derivatives. This will require tweaking the time integration so that $\partial\rho/\partial t$ becomes small while the other four time derivatives remain relatively untouched. The numerical scheme integrates the five dependent variables, ρ, ρv_x, ρv_y, ρv_z, and E [see Eqs. (11)–(13)]. We can write an integration step for a typical quantity q as

$$q^{n+1}=q^n+C\times\Delta t\times\partial q/\partial t. \tag{A1}$$

For $q=\rho$, we increased *C* above unity, each time relaxing the flow and measuring the time period of the oscillations. This means that the density should vary over a longer time scale than the other quantities.

Consider the simulation $Z=0.32$, $m=1.5$. This had an oscillation period of 70 sound travel times. We find that for *C* equal to 1, 1.5, 1.75, and 2.0, the oscillation period is 70, 50, 44, and 40, sound travel times. When $C=1$, we are solving the fully compressible Navier–Stokes equations, and as *C* is increased the equations should behave more and more like the anelastic equations. Figure 11 shows $(\partial\rho/\partial t)_{\rm rms}$ divided by the depth average of $(\rho\nabla\cdot\mathbf{v})_{\rm rms}$ versus height. As *C* increases, the relative size of $\partial\rho/\partial t$ term is getting smaller and smaller. This is especially true near the horizontal boundaries.

For each value of *C*, the relative thermodynamic fluctuations (not shown) were always less than 0.1, and the corresponding oscillation period is within a factor of 2 of the convective turn-over time. These oscillation periods are at least 40 times greater than the sound travel time. Under such conditions, the anelastic equations should be able to predict the same results as the fully compressible equations (i.e., an oscillation period of 70). But these preliminary results suggest otherwise.

[1] X.-Z. Wu and A. Libchaber, "Non-Boussinesq effects in free thermal convection," Phys. Rev. A **43**, 2833 (1991).
[2] J. J. Niemela, L. Skrbek, K. R. Sreenivasan, and R. J. Donnelly, "Turbulent convection at very high Rayleigh numbers," Nature (London) **404**, 837 (2000).
[3] G. T. Jarvis and D. P. Mckenzie, "The conversion of heat into mechanical work by mantle convection," J. Geophys. Res. **85**, 6093 (1980).
[4] J. Zhang, S. Childress, and A. Libchaber, "Non-Boussinesq effect: Asymmetric velocity profiles in thermal convection," Phys. Fluids **10**, 1534 (1998).
[5] X. Chavanne, F. Chila, B. Chabaud, B. Castaing, and B. Hébral, "Turbulent Rayleigh–Bénard convection in gaseous and liquid He," Phys. Fluids **13**, 1300 (2001).
[6] J. J. Niemela and K. R. Sreenivasan, "Confined turbulent convection," J. Fluid Mech. **481**, 355 (2003).
[7] J. Boussinesq, *Theory Analytique de la Chaleur* (Gauthier-Villars, Paris, 1903), Vol. 2.
[8] J. P. Gollub and S. V. Benson, "Many routes to turbulent convection," J. Fluid Mech. **100**, 449 (1980).

[9]R. Farhadieh and R. R. Tankin, ''Interferometric study of two-dimensional Bénard convection cells,'' J. Fluid Mech. **56**, 739 (1974).
[10]F. B. Lipps, ''Numerical simulation of three-dimensional Bénard convection in air,'' J. Fluid Mech. **75**, 113 (1976).
[11]E. Bodenschatz, W. Pesch, and G. Ahlers, ''Recent developments in Rayleigh–Bénard convection,'' Annu. Rev. Fluid Mech. **32**, 709 (2000).
[12]J. Zhang, S. Childress, and A. Libchaber, ''Non-Boussinesq effect: Thermal convection with broken symmetry,'' Phys. Fluids **9**, 1034 (1997).
[13]A. Roy and V. Steinberg, ''Reentrant hexagons in non-Boussinesq Rayleigh–Benard convection: Effect of compressibility,'' Phys. Rev. Lett. **88**, 244503 (2002).
[14]H. Meyer and A. B. Kogan, ''Onset of convection in a very compressible fluid: The transient toward steady state,'' Phys. Rev. E **66**, 056310 (2002).
[15]H. Meyer and A. B. Kogan, ''Oscillatory and relaxation studies in the convection of supercritical He-3,'' Physica B **329**, 114 (2003).
[16]K. T. Yang, ''Transitions and bifurcations in laminar buoyant flows in confined enclosures,'' ASME J. Heat Transfer **110**, 1204 (1988).
[17]V. E. Denny and R. M. Clever, ''Comparisons of Galerkin and finite difference methods for solving highly nonlinear thermally driven flows,'' J. Comput. Phys. **16**, 271 (1974).
[18]D. O. Gough, D. R. Moore, E. A. Spiegel, and N. O. Weiss, ''Convective instability in a compressible atmosphere II,'' Astrophys. J. **206**, 536 (1976).
[19]F. H. Busse, ''Nonlinear properties of thermal convection,'' Rep. Prog. Phys. **41**, 1967 (1978).
[20]M. C. Depassier and E. A. Spiegel, ''The large-scale structure of compressible convection,'' Astron. J. **86**, 496 (1981).
[21]F. H. Busse and R. M. Clever, ''Mechanisms of the onset of time-dependence in thermal convection,'' *Time-Dependent Nonlinear Convection*, edited by P. A. Tyvand (Computational Mechanics, Southampton, UK, 1998), pp. 1–50.
[22]D. Mukutmoni and K. T. Yang, ''Rayleigh–Bénard convection in a small aspect ratio enclosure: Part 1—Bifurcation to oscillatory convection,'' ASME J. Heat Transfer **115**, 360 (1993).
[23]N. E. Hurlbert, J. Toomre, and J. M. Massaguer, ''Two-dimensional compressible convection extending over multiple scale heights,'' Astrophys. J. **282**, 557 (1984).
[24]E. Graham, ''Numerical simulation of two-dimensional compressible convection,'' J. Fluid Mech. **70**, 689 (1975).
[25]S. Paolucci and D. R. Chenworth, ''Departures from the Boussinesq approximation in laminar Bénard convection,'' Phys. Fluids **30**, 1561 (1987).
[26]J. Fröhlich, P. Laure, and R. Peyret, ''Large departures from Boussinesq approximation in the Rayleigh–Bénard problem,'' Phys. Fluids A **4**, 1355 (1992).
[27]K. L. Chan and C. L. Wolff, ''ADI on a staggered mesh—A method for the calculation of compressible convection,'' J. Comput. Phys. **47**, 109 (1982).
[28]G. K. Batchelor, *An Introduction to Fluid Mechanics* (Cambridge University Press, Cambridge, UK, 1988).
[29]F. J. Robinson, P. Demarque, L. H. Li, S. Sofia, Y.-C. Kim, K. L. Chan, and D. B. Guenmther, ''Three-dimensional convection simulations of the outer layers of the Sun using realistic physics,'' Mon. Not. R. Astron. Soc. **340**, 923 (2003).
[30]R. P. Behringer, ''Rayleigh–Bénard convection and turbulence in liquid helium,'' Rev. Mod. Phys. **57**, 657 (1985).
[31]P. Colinet and J. C. Legros, ''On the Hopf bifurcation occurring in the two-layer Rayleigh–Bénard convective instability,'' Phys. Fluids **6**, 2631 (1994).
[32]J. P. Gollub, S. V. Benson, and J. F. Steinman, ''A subharmonic route to turbulent convection,'' *Nonlinear Dynamics*, edited by H. G. Hellman (New York Academy of Sciences, New York, 1980).
[33]W. V. R. Malkus and G. Veronis, ''Finite amplitude cellular convection,'' J. Fluid Mech. **4**, 225 (1958).
[34]D. J. Tritton, *Physical Fluid Dynamics* (Oxford University Press, New York, 1988).
[35]E. W. Bolton, F. H. Busse, and R. M. Clever, ''Oscillatory instability of convection rolls at intermediate Prandtl numbers,'' J. Fluid Mech. **164**, 469 (1986).
[36]F. H. Busse and R. M. Clever, ''Standing and traveling oscillatory blob convection,'' J. Fluid Mech. **297**, 255 (1995).
[37]J. J. Niemela (personal communication).
[38]R. J. Donnelly, ''Ultrahigh Reynolds number flows using cryogenic helium: An overview,'' *Flow at Ultrahigh Reynolds and Rayleigh Numbers: A Status Report*, edited by R. J. Donnelly and K. R. Sreenivasan (Springer, Berlin, 1998).
[39]G. K. Batchelor, ''The conditions for dynamical similarity of motions of motions of a frictionless perfect-gas atmosphere,'' Q. J. R. Meteorol. Soc. **79**, 224 (1953).
[40]R. Van der Borght and P. Fox, ''Accuracy of the anelastic approximation in the theory of compressible convection,'' Proc. ASA **5**, 170 (1983).